Nano Research

Open Access

Research Article

Surface lattice engineering of CdO/CdS nano-heterostructure modulated by electron beam irradiation

Yumin Wang[1], Yi Xiong[2], Wei Zeng[3], and Pengfei Fang[1] ✉

[1] School of Physics and Technology, Key Laboratory of Nuclear Solid State Physics Hubei Province, Wuhan University, Wuhan 430072, China
[2] Analytical and Testing Center, Key Laboratory of Textile Fiber and Products, Ministry of Education, National Local Joint Engineering Laboratory for Advanced Textile Processing and Clean Production, Wuhan Textile University, Wuhan 430073, China
[3] Information Materials and Intelligent Sensing Laboratory of Anhui Province, Anhui University, Hefei 230601, China

Cite this article: *Nano Research*, **2025**, *18*, 94907001. https://doi.org/10.26599/NR.2025.94907001

ABSTRACT: In-depth research on structural transformations induced by electron beam will be helpful for the design and manufacture of nanostructures. The nucleation and growth mechanism of CdO nanocrystals on CdS matrix was studied through *in situ* transmission electron microscopy observation. The results of energy dispersive spectrum reveal the electron beam induced surface oxidation of CdS. CdO nanocrystals nucleate through a non-classical two-step nucleation path on CdS surface. Amorphous cluster forms first as the intermediate phase in the two-step nucleation of CdO nanocrystals. Then unstable crystal nucleus is formed in the amorphous phase, accompanied by reversible disorder–order transitions. After absorbing the amorphous phase and rapidly growing, the CdO nucleus grows through the classic layer-by-layer growth mechanism. Furthermore, six nonequivalent heterojunction interface orientation relationships between CdO nanocrystals and CdS matrix were deeply analyzed. This work demonstrates potential application prospects for atomic manufacturing and interface control of semiconductor heterojunction.

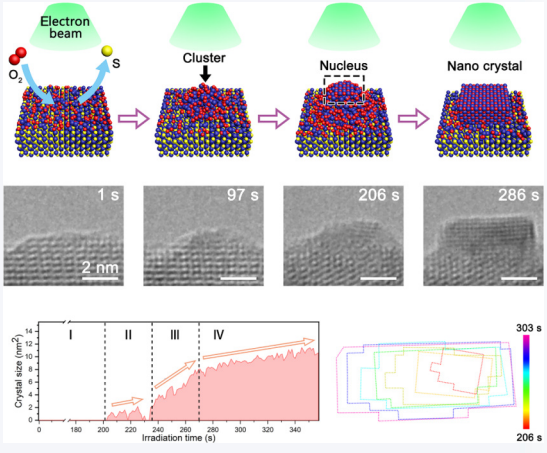

KEYWORDS: surface oxidiation, electron beam irradiation, two-step nucleation mechanism, nano-heterostructure

1 Introduction

With the widespread use of nanocrystals in scientific research fields such as photocatalysis, photonics devices, and drug preparations [1–5], the study on nucleation and growth mechanism of nanocrystals is receiving increasing attention. Factors such as crystal size, crystal structure, defect concentration, and heterojunction interface, which significantly affect material properties, are determined by the crystal nucleation and growth process [6–10]. Usually, nucleation and growth theories of crystals can be divided into two categories: classical theory and non-classical theory. In classical theory, a crystal nucleus is formed by the aggregation of monomers (atoms, ions, or molecules) in space and remains stable after its free energy exceeds the nucleation energy barrier, then the crystal nucleus grows by building new facets on surface [11, 12]. As a supplement to classical theory, non-classical theory aims to explain crystallization behaviors beyond classical category. Non-classical nucleation often involves intermediate phases, such as pre-nucleation clusters, primary particles, and amorphous phase, while non-classical growth mainly involves the oriented attachment and fusion between crystal nuclei [12–15]. Up to now, non-classical crystallization has shown broad application potential in functional materials, energy materials, pharmaceutics, and medicine fields [13].

Two-step nucleation is a common non-classical nucleation method. The main feature of this nucleation method is the formation of an intermediate phase (mostly amorphous phase) first, followed by further nucleation in the intermediate phase [12–14]. Currently, many studies focus on two-step nucleation of organic molecules in liquid phase [16–20]. In fact, two-step nucleation also exists in solid-phase inorganic materials, such as two-step nucleation of amorphous iron oxides under heating condition [21], two-step nucleation of metal crystal nucleus in single-walled carbon nanotubes [22], and two-step nucleation of Bi particles on two

Received: June 30, 2024; **Revised:** August 23, 2024
Accepted: August 25, 2024

✉Address correspondence to fangpf@whu.edu.cn

matrices [23]. The study of two-step nucleation in solid-state inorganic materials (especially on the surface and interface) will promote the further development of two-step nucleation theory.

The electron beam in transmission electron microscopy (TEM) can induce some structural transformations, such as phase transition [24], nanopore formation [25], nanowire growth [26], and crystallization of amorphous nanoparticles [27]. Besides these, electron beam induced surface oxidation of metals and semiconductors is also a current research focus. Examples include electron beam induced oxidation of Ag [28] and *in situ* growth of In_2O_3 nanocrystals on In_2S_3 nanosheets [29]. Thus, the electron beam is an effective and promising tool for manufacturing and controlling nanostructures [30]. Considering the significant effect of nanostructure on material properties, the research focused on electron beam induced structure evolution is of great scientific promise.

As a typical II–VI group compound with great photoelectric properties, CdS is commonly used to construct photocatalysts and semiconductor devices [31, 32]. Loading CdO nanocrystals on CdS matrix is an effective method to improve photoelectric performance [33–35]. Interestingly, electron beam can induce direct growth of CdO nanocrystals on the surface of CdS. In 2016, Huang et al. observed electron beam induced surface oxidation of CdS nanobelt to form CdO nanocrystals through high-resolution TEM (HRTEM). And they found that carbon deposition and heating can inhibit the oxidation process of CdS nanobelt [36]. However, the nucleation and growth mechanism of CdO nanocrystals based on surface oxidation remains a mystery. Assisting in the design and regulation of CdO/CdS nano-heterojunction materials requires in-depth research on the crystallization process of CdO.

Herein, we investigated the nucleation and growth of CdO nanocrystals during electron beam induced surface oxidation of CdS nanowires. The electron beam induced surface oxidation of CdS was revealed through long-term electron beam irradiation experiment. By analyzing the HRTEM images and movies captured in the electron beam irradiation experiment, we proposed the two-step nucleation model of CdO nanocrystals, and studied six nonequivalent heterojunction interface orientation relationships between CdO nanocrystals and CdS matrix. This work is beneficial for manufacturing of nano materials and structural design of heterojunction devices.

2 Experimental

CdS nanowires were prepared according to the method described in our previous work [37]. X-ray diffractometer (XRD, PANalytical Empyrean) was used to characterize the crystal structure of CdS nanowires. The morphology images of the initial CdS nanowires were captured using scanning electron microscopy (SEM, SU-5000), and the crystal lattice images were captured using HRTEM (JEM-2100Plus). In addition, energy dispersive spectrum (EDS) was used to capture the element mapping images. In the electron beam irradiation experiment, the CdS nanowires were exposed to an electron beam with an accelerating voltage of 200 kV and a current density of 4.8 A/cm^2. Under the electron beam irradiation, the HRTEM images and movies of CdS nanowires were captured by the charge-coupled device (CCD) camera. In long-term electron beam irradiation experiment, the CdS nanowires were exposed to the constant electron beam irradiation for a total of 20 min, with element content measured every 2 min using EDS. And selected area electron diffraction (SAED) patterns of the initial and final CdS nanowires were captured in this experiment.

3 Results and discussion

As shown in the XRD spectrum (Fig. S1 in the Electronic Supplementary Material (ESM)), the characteristic diffraction peaks completely correspond to the wurtzite (WZ) phase CdS (JCPDS Card No. 41–1049), and sharp diffraction peaks indicate good crystallinity of prepared CdS nanowires. The SEM images (Fig. S2 in the ESM) show the morphology of CdS nanowires, which are elongated crystals with the length typically exceeding 1 μm and the width of 40–50 nm. Then, the CdS nanowires were observed using TEM at a low electron irradiation dose to ensure minimal damage from electron beam irradiation. As shown in Fig. 1(a), the CdS nanowires exhibit elongated strip-like morphology and are aggregated into a bunch. The long strip structure of CdS nanowires makes them vulnerable to stress and bending, which results in structural bending and the generation of interference fringes. Figure 1(b) shows the HRTEM of a single CdS nanowire, indicating the [0001] crystal orientation of WZ CdS. Figure S3 in the ESM shows the HRTEM image of CdS surface with clean and intact surface lattice. Figure 1(c) is a zoom-in image of the boxed area in Fig. 1(b), which clearly shows the $(10\bar{1}0)$ crystal plane with the lattice spacing of 3.60 Å and the (0002) crystal plane with the lattice spacing of 3.37 Å of the WZ CdS matrix. Figure 1(d) is the fast Fourier transform (FFT) pattern of Fig. 1(c), which correspond well to WZ CdS in the $[\bar{1}2\bar{1}0]$ zone axis direction. Figure 1(e) shows the scanning transmission electron microscopy (STEM) image of CdS nanowires, and Figs. 1(f)–1(h) show the corresponding EDS element mapping images. Cd and S are uniformly distributed on the nanowires, and their contents are close to 1:1 (shown in Fig. S4 in the ESM). The small amount of O signal (relative content is 1.9%, as shown in Fig. S4 in the ESM) is believed to originate from the O species adsorbed on the surface of CdS [36]. Based on above results, the CdS nanowires prepared in this paper are slender single crystals with WZ structure, having certain O species adsorbed on their surface.

During TEM observation, the morphology of CdS nanowires

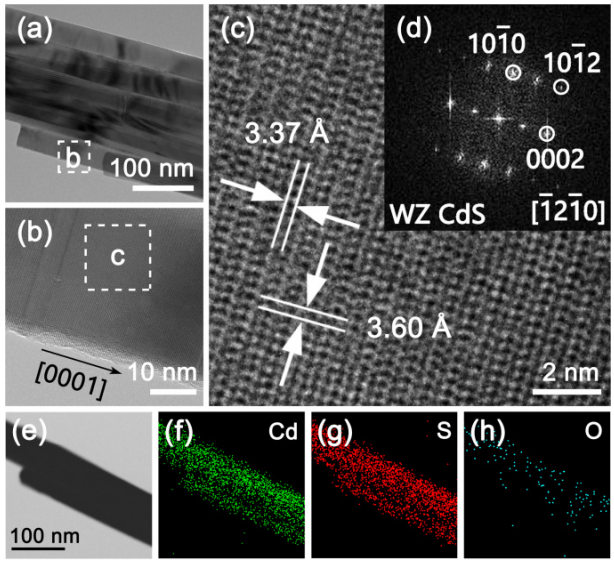

Figure 1 (a) TEM image of CdS nanowires. (b) HRTEM image of single CdS nanowire corresponding to the boxed area in (a). (c) Zoom-in image of the boxed area in (b) showing the crystal lattice of WZ CdS. (d) The FFT pattern of the WZ CdS lattice. (e) STEM image of CdS nanowires and (f)–(h) corresponding EDS element mapping images of Cd, S, and O.

underwent structural evolution with electron beam irradiation. Three HRTEM movies (Movies S1–S3 in the ESM) were taken under the electron beam irradiation with an accelerating voltage of 200 kV and a current density of 4.8 A/cm^2 to analyze the structural evolution of CdS nanowires. Several images from Movie S1 in the ESM are shown in Fig. 2. Initially, the surface of the CdS nanowire is almost flat as shown in Fig. 2(a). After 25 s electron beam irradiation (Fig. 2(b)), significant protrusions (marked by arrows) appear at the surface of CdS. After 36 s electron beam irradiation (Fig. 2(c)), some new crystal nuclei form at the protrusions. After 51 s electron beam irradiation (Fig. 2(d)), these crystal nuclei further grow to form nanocrystals (marked by arrows). Rate of this structural evolution is positively correlated with the current intensity of electron beam (shown in Fig. S5 in the ESM), which means these processes are induced by electron beam.

Figures 2(e)–2(h) are zoom-in images of the corresponding marked areas in Figs. 2(a)–2(d). Figure 2(e) shows a zoom-in image of the boxed area in Fig. 2(a), in which a small amount of amorphous phase on the surface of CdS can be observed. Then in Fig. 2(f), an amorphous cluster forms on the surface of CdS. After a certain period of irradiation, new crystal nucleus appears in the amorphous cluster in Fig. 2(g). And in Fig. 2(h), this crystal nucleus grows into a nanocrystal, which can be identified as a CdO nanocrystal with rock salt (RS) structure based on its clear lattice. The dissociation energy of CdO is higher than that of CdS [38], which makes CdO more stable under electron beam irradiation and conducive to its formation. The lattice spacing of 2.34 Å corresponds to (002) crystal plane of RS CdO and the lattice spacing of 2.70 Å corresponds to (111) crystal plane of RS CdO. This CdO nanocrystal is labeled as NC-1. Figure 2(i) is the FFT pattern of NC-1, which corresponds well to RS CdO in the [1$\bar{1}$0] zone axis direction.

To investigate the effect of long-term electron beam irradiation on CdS nanowires, some CdS nanowires were irradiated by electron beam for 20 min. Figures 3(a)–3(d) show the TEM images of CdS nanowires during the long-term electron beam irradiation. Initial CdS nanowires in Fig. 3(a) have smooth surface. As the irradiation time increases, the deformation of the nanowires becomes increasingly severe. After 4 min electron beam irradiation (Fig. 3(b)), many CdO nanocrystals appear on the surface of CdS nanowires. As the irradiation time increases, CdO nanocrystals will further grow along the CdS surface, and adjacent CdO nanocrystals will contact each other and form a grain boundary (as shown in Fig. S6 in the ESM). In Fig. S7 in the ESM, due to the misorientation in the crystal orientation (about 9.8° in Fig. S7(c) in the ESM) of adjacent CdO nanocrystals, their lattices cannot be completely aligned, resulting in the formation of the low angle grain boundary between them. The morphology of CdS nanowires with CdO polycrystalline layer formed on the surface is shown in Fig. 3(c). Then the thickness of the CdO polycrystalline layer continues to increase (Fig. 3(d)). Meanwhile, some holes will form between the CdO nanocrystals and CdS matrix, disrupting the CdO/CdS nano-heterostructure (as shown in Fig. S8 in the ESM). Figure 3(e) shows the SAED image of initial CdS nanowires. Due to the highly uniform crystal orientation of the aggregated CdS nanowires, the diffraction lattice of WZ CdS in the [1$\bar{2}$10] zone axis direction is clearly observed in Fig. 3(e). In Fig. 3(f), the RS CdO diffraction rings can be observed after long-term electron beam irradiation, while the diffraction lattice of WZ CdS still exists. The relative element content of nanowires with different irradiation times was measured by EDS in the long-term electron beam irradiation experiment. As shown in the EDS spectrum (Fig. 3(g)), the peak of element O (marked by black box) increases with the increase of irradiation time, and the peak of element S (marked by black box) decreases with the increase of irradiation time. The peak of Cd element remains almost unchanged. The peak of Cu element comes from the microgrid and its intensity remains unchanged during irradiation. Also, the weak peak of C element originates from the carbon film on the microgrid. Figure 3(h) shows the relative atomic content percentage of Cd, S, and O during the electron beam irradiation. The relative atomic content percentage of O increases with the increase of irradiation time, while the relative atomic content percentage of S decreases with the increase of irradiation time. The relative atomic content percentage of Cd is basically stable, and its slight changes are mainly due to the fluctuation of the total atomic number of these three elements during the irradiation experiment. EDS analysis results indicate the atomic exchange between CdS nanowires and the vacuum within the TEM. The

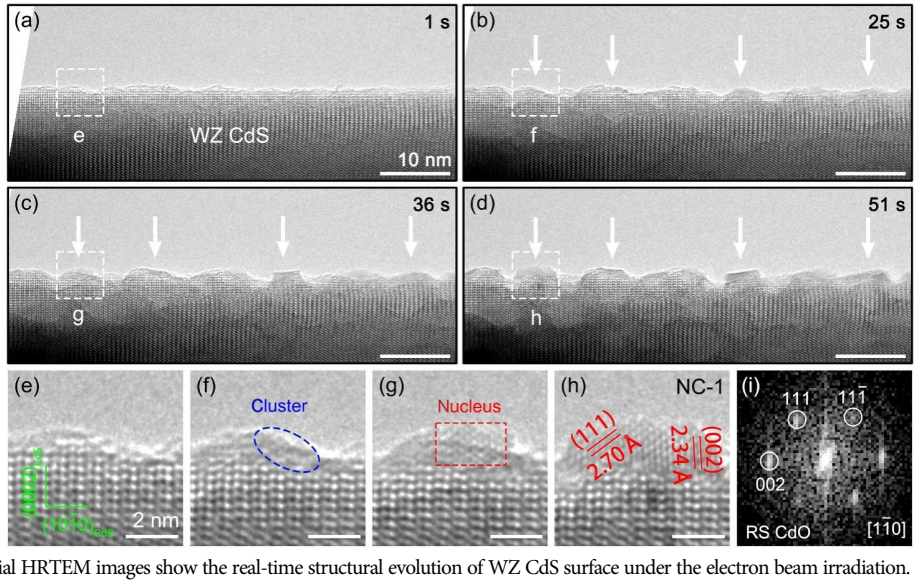

Figure 2 (a)–(d) Sequential HRTEM images show the real-time structural evolution of WZ CdS surface under the electron beam irradiation. (e)–(h) Zoom-in images of the corresponding marked areas show the WZ CdS surface, amorphous cluster, crystal nucleus, and RS CdO nanocrystal. (i) FFT pattern of the RS CdO nanocrystal.

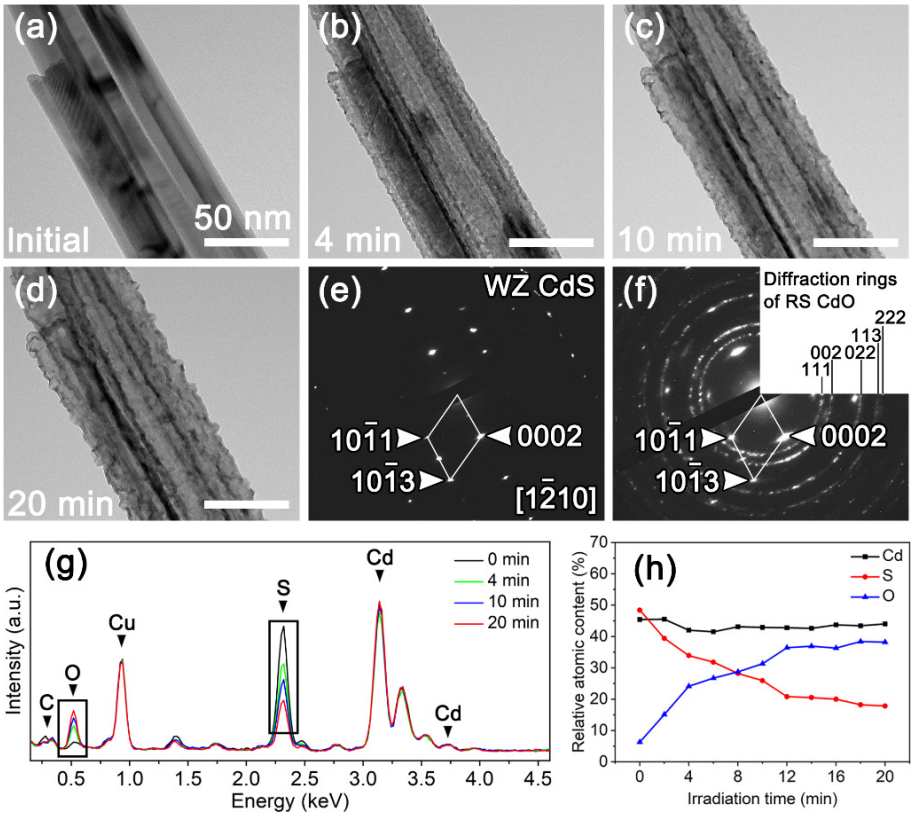

Figure 3 (a)–(d) TEM images showing the initial CdS nanowires and the CdS nanowires irradiated by electron beam for 4, 10, and 20 min. (e) and (f) SAED images of initial CdS nanowires and the CdS nanowires irradiated by the electron beam for 20 min. (g) EDS spectra and (h) relative atomic content of CdS nanowires with different irradiation times.

S atoms on the CdS surface escape into the vacuum, while the O species in the vacuum adsorb onto the CdS surface and are fixed in the form of CdO nanocrystals under the action of electron beam irradiation. The O species initially adsorbed on the surface of CdS will participate in the early nucleation process. In addition, excessive oxidation severely damages the surface structure of nanowires, thus study on the formation mechanism of CdO nanocrystals is necessary for the regulating of oxidation process.

Sequential HRTEM images from Movie S2 in the ESM demonstrate the nucleation and growth process of a CdO nanocrystal. Figure 4(a) shows the CdS surface (colored in green) recorded in the first second, with a small amount of amorphous phase (colored in blue) adsorption. The small amount of amorphous phase on the surface is due to low-dose electron beam irradiation on CdS nanowires before the photography. The surface lattice of the initial CdS nanowire is clean and intact (as shown in Fig. S3 in the ESM). At 97 s (Fig. 4(b)), the amorphous phase slightly increases and aggregates to form a cluster. At 192 s (Fig. 4(c)), the amorphous phase grows into a cluster approximately 1.5 nm thick and 5 nm long. At 206 s (Fig. 4(d)), a crystal nucleus of RS CdO (colored in red) appears in the amorphous cluster. Over time, the crystalline phase grows in the amorphous phase (shown in Fig. 4(e)). Until 286 s (Fig. 4(f)), most of the amorphous phase transforms into crystalline phase. The CdO nanocrystal shown in Fig. 4(f) is labeled as NC-2. An additional movie (Movie S4 in the ESM) depicts the formation process of NC-2. Clearly, amorphous clusters serve as the intermediate phase in the nucleation of CdO nanocrystals. This nucleation process can be classified as two-step nucleation, a non-classical nucleation path [13, 14]. Similar two-step nucleation mechanisms were found in the nucleation processes of Ni nanocrystals and Bi nanocrystals [23, 39, 40]. An undeniable aspect is the decomposition of CdS matrix. As shown in Fig. S9 in the ESM, the decomposition of CdS leads to the formation and evolution of surface atomic steps. Surface atomic steps can form various defect structures during the evolution process, which serve as nucleation sites for CdO nanocrystals and affect their nucleation process. Upon continuous irradiation, the CdS matrix continuously decomposes from the surface, resulting in the formation of defective structures. In Fig. S10 in the ESM, sequential HRTEM images from Movie S2 in the ESM and corresponding filtering images show the decomposition of CdS surface. Additionally, the CdO nanocrystal in the Fig. 4(f) has a slight curvature, which can be attributed to the stress generated by interface lattice mismatch, such as the atomic step (marked by white line) at the interface between the CdO nanocrystal and the CdS matrix.

Based on the above analysis results, atomic models for the nucleation and growth of CdO nanocrystals on the CdS surface induced by electron beam are established (Fig. 4(g)). The surface S vacancies have the smallest formation energy [41], which makes it easy for surface S atoms to sputter into vacuum under electron beam irradiation. After the electron beam begins to irradiate the sample, CdS is subjected to knock-on damage under the irradiation of the electron beam, and the S atoms in its surface lattice are ejected into vacuum, while O spacies (using O_2 as an example) adsorb onto the surface of CdS and form chemical bonds with excess Cd atoms. Driven by electron beam irradiation, disordered O atoms and Cd atoms on the surface of CdS migrate and agglomerate to form an amorphous cluster, thereby reducing

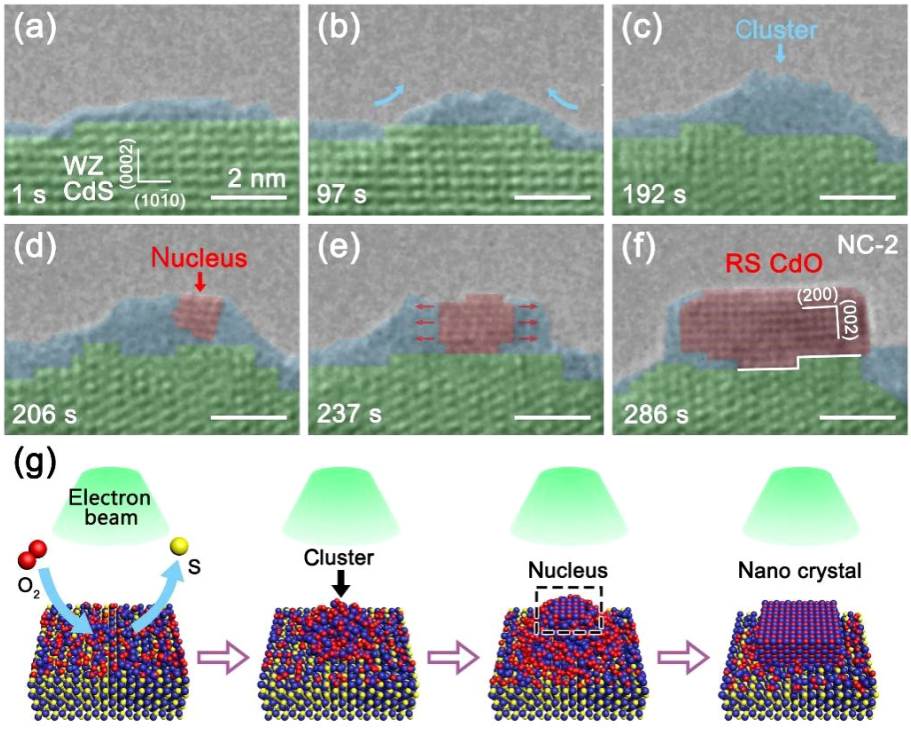

Figure 4 (a)–(c) Sequential HRTEM images show the amorphous phase (colored in blue) aggregation to form a cluster on the WZ CdS surface (colored in green). (d)–(f) Sequential HRTEM images show the growth of the RS CdO crystal nucleus (colored in red). (g) Schematic showing the nucleation and growth of RS CdO nanocrystal.

surface energy. Cd atoms mainly migrate through interstitial diffusion in the lattice and eventually come to the surface to participate in the formation of CdO nanocrystals [42]. Electron beam irradiation induces ordered arrangement of atoms in amorphous cluster to form a RS CdO crystal nucleus. Then the CdO crystal nucleus converts amorphous cluster into a CdO nanocrystal.

Figure 5 shows the further analysis results of crystallization process of the CdO nanocrystal (NC-2). As shown in Fig. 5(a), the CdO crystal nucleus undergoes reversible disorder–order transitions in the early crystal nucleation stage. From 200 to 206 s, a crystal nucleus forms in the amorphous phase. From 206 to 210 s, the crystallization area reduces in size. From 210 to 216 s, the CdO crystal nucleus grows larger. At 218 s, the CdO crystal nucleus disappears. Then at 225 s, the amorphous phase crystallizes again. Similar phenomena have been reported in nucleation of Au nanocrystals and Bi nanocrystals [23, 43]. The reversible disorder–order transitions are due to the high nucleation free energy of the CdO crystal nucleus in the early nucleation stage. The formation of CdO nuclei in the amorphous phase is a result of heterogeneous nucleation. The defects on the interface play an important role as nucleation sites in the nucleation process of CdO nanocrystals. Figure 5(b) shows the layer-by-layer growth of the CdO nanocrystal. At 241 s, the CdO nanocrystal has six (002) planes and a growing half plane. After the formation of new crystal plane, the CdO nanocrystal has seven (002) planes at 250 s. Then at 262 s, a new half plane appears on the top of the CdO nanocrystal. Therefore, the CdO nanocrystal is believed to grow via the classic layer-by-layer growth mechanism after nucleation, with the (002) plane as the predominant growth facet.

Figure 5(c) shows the function curve of CdO crystal size variation with irradiation time. Based on this function curve and Movie S4 in the ESM, the nucleation and growth of the CdO nanocrystal can be divided into four stages. In stage I, amorphous phase aggregates to form a cluster on CdS surface. In stage II, a tiny CdO crystal nucleus forms in the amorphous cluster. At this stage, the crystal size of CdO nuclei fluctuates significantly. In stage III, the CdO crystal nucleus grows rapidly by absorbing amorphous phase. In stage IV, most of the amorphous phase disappear while the growth rate of CdO nanocrystal slows down. Figure 5(d) shows the time-labeled contours of the CdO nanocrystal from 206 to 303 s. In the crystal nucleation stage, CdO nanocrystal underwent a small angle rotation to form stable contact with the CdS surface. As show in Fig. S11 in the ESM, the CdS nanocrystal rotated by approximately 8.0° from 206 to 247 s. Furthermore, as shown in Fig. S11(f) in the ESM, the crystal orientation of this CdO nanocrystal fluctuates significantly from 206 to 228 s (corresponding to stage II), while it fluctuates slightly from 235 to 251 s (corresponding to stage III). This result also indicates that stage II is an unstable nucleation stage. Figure S12 in the ESM shows the crystal growth curve of NC-1, which is similar to that of NC-2 (as shown in Fig. 5(c)). This indicates that the growth mode of NC-2 is not accidental. In addition, the CdO nucleus approximates a square shape in the early stage of nucleation, but it assumes a rectangular shape as it grows. This means that the CdO nanocrystal grows mainly in the $[001]_{CdO}$ direction rather than in the $[100]_{CdO}$ direction, even though these two directions are equivalent to the CdO nanocrystal in crystallography. This growth tendency is likely due to the difficulty of Cd atoms migrating to areas far from CdS surface.

Except for NC-1 and NC-2, Fig. 6 shows the two-step nucleation and oriented growth of four CdO nanocrystals with different crystal orientations on CdS surface. Figure 6(a) originates from Movie S2 in the ESM and Figs. 6(b)–6(d) originate from Movie S3 in the ESM. In Fig. 6(a), the amorphous cluster forms on the atomic slope

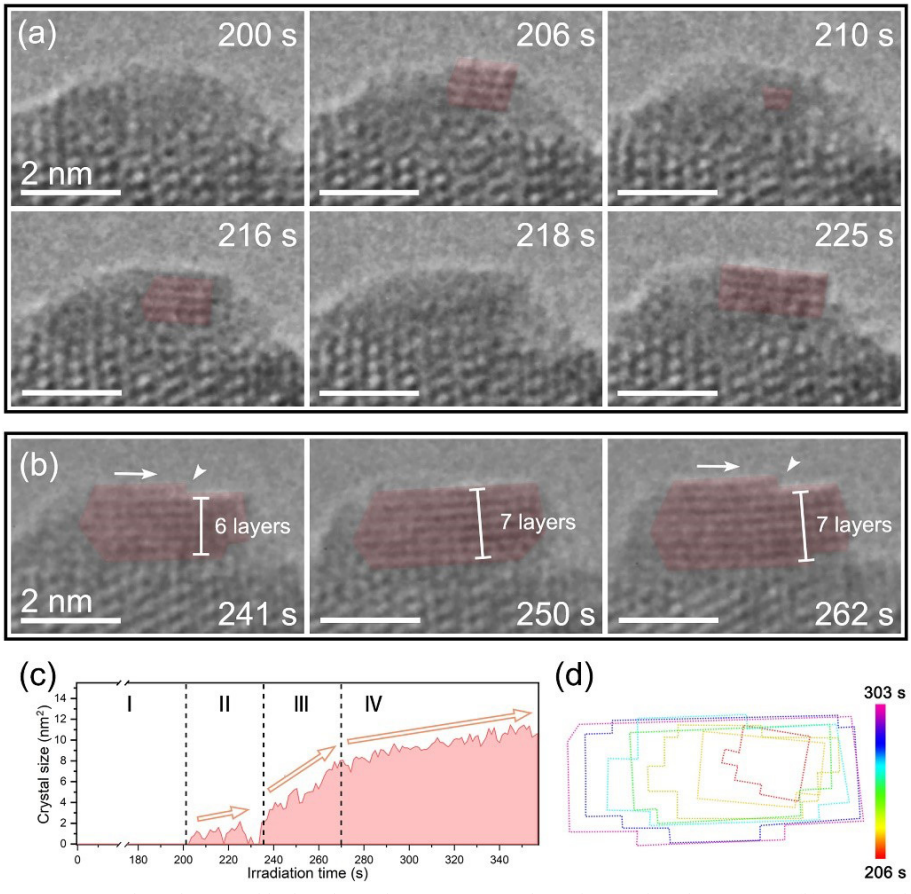

Figure 5 (a) Sequential HRTEM images show the reversible disorder–order transitions in the early crystal nucleation stage. (b) Sequential HRTEM images show the layer-by-layer growth of CdO nanocrystal. (c) Crystal size of the CdO nanocrystal (NC-2) as the function of the irradiation time. (d) Time-labeled contours of the CdO nanocrystal.

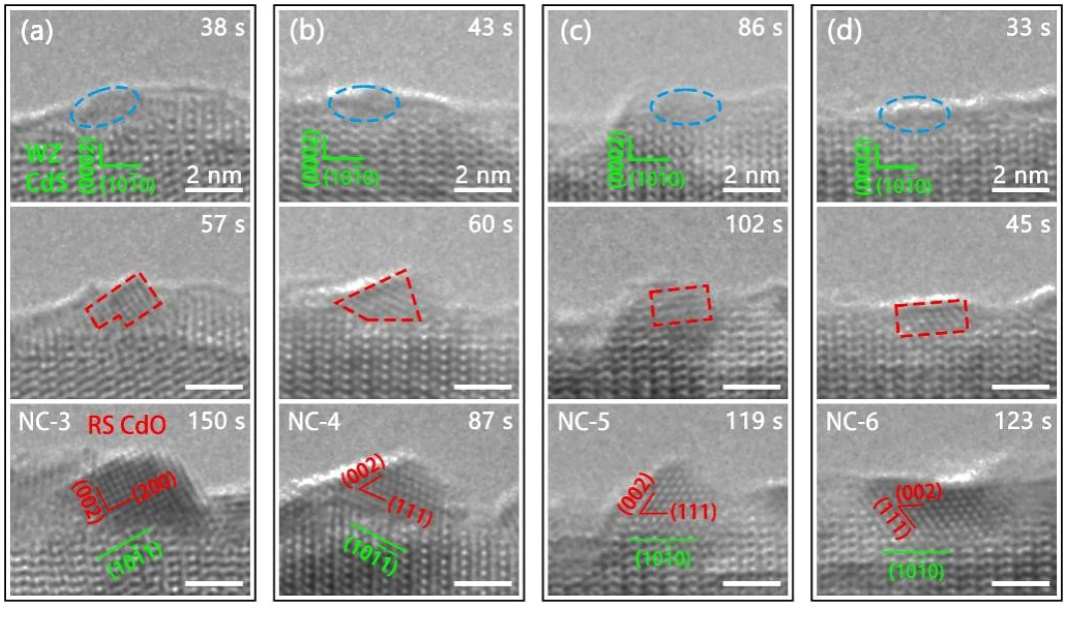

Figure 6 HRTEM images show the nucleation and growth of RS CdO nanocrystals: (a) NC-3, (b) NC-4, (c) NC-5, and (d) NC-6.

of CdS surface, then it undergoes crystallization to form a CdO nanocrystal (labeled as NC-3), while $(200)_{CdO}$ plane is parallel to $(10\bar{1}1)_{CdS}$ plane. In Fig. 6(b), the amorphous cluster forms at a concave defect of CdS matrix, then it transforms into a CdO nanocrystal (labeled as NC-4), while $(111)_{CdO}$ plane is parallel to $(10\bar{1}\bar{1})_{CdS}$ plane. Note that the main crystal planes ({002} plane, {111} plane, and {220} plane) of NC-3 and NC-4 are not parallel to the $(10\bar{1}0)_{CdS}$ plane. Due to the decomposition of CdS matrix, the $\{10\bar{1}1\}_{CdS}$ planes appear on the surface of CdS through the formation and evolution of surface atomic steps. $\{10\bar{1}1\}_{CdS}$ planes in

Figs. 6(a) and 6(b) are in direct contact with amorphous clusters, which leads to the oriented growth of CdO nanocrystals along the $\{10\bar{1}1\}_{CdS}$ plane. The amorphous clusters in Figs. 6(c) and 6(d) also form at concave defects of CdS matrix, and they transform into CdO nanocrystals with different crystal orientations on CdS surface. The CdO nanocrystal in Fig. 6(c) is labeled as NC-5, while $(111)_{CdO}$ plane is parallel to $(10\bar{1}0)_{CdS}$ plane. The CdO nanocrystal in Fig. 6(d) is labeled as NC-6, while $(002)_{CdO}$ plane is parallel to $(10\bar{1}0)_{CdS}$ plane. Lattice defects on CdS surface may be an important factor affecting the oriented growth of CdO nanocrystals, such as the exposed atomic slope can induce CdO nanocrystals to grow along the inclined direction.

These six CdO nanocrystals shown earlier have nonequivalent crystal orientation relationships with CdS matrix, and only one of them has been reported in relevant Ref. [36]. Interface lattice matching between these six CdO nanocrystals and CdS $(10\bar{1}0)$ plane was analyzed and the result is shown in Fig. 7. Moreover, corresponding atomic models were constructed to furtherly analyze the crystal orientation relationship between CdO nanocrystals and CdS matrix. In Fig. 7(a), $(002)_{CdO}$ plane is parallel to $(0002)_{CdS}$ plane while $(220)_{CdO}$ plane is parallel to $(10\bar{1}0)_{CdS}$ plane, and $[1\bar{1}0]_{CdO}$ zone axis is parallel to $[\bar{1}2\bar{1}0]_{CdS}$ zone axis. In Fig. 7(b), $(002)_{CdO}$ plane is parallel to $(0002)_{CdS}$ plane while $(200)_{CdO}$ plane is parallel to $(10\bar{1}0)_{CdS}$ plane, and $[010]_{CdO}$ zone axis is parallel to $[\bar{1}2\bar{1}0]_{CdS}$ zone axis. For NC-1 and NC-2, ten $(002)_{CdO}$ layers match to seven $(0002)_{CdS}$ layers on the interface. Additionally, the d-spacing of two $(220)_{CdO}$ layers (3.30 Å) is relatively close to that of one $(10\bar{1}0)_{CdS}$ layer (3.61 Å), which makes NC-1 less prone to bending due to atomic steps at the interface. But for NC-2, the d-spacing of $(200)_{CdO}$ plane (2.34 Å) is far from that of $(10\bar{1}0)_{CdS}$ plane (3.61 Å), which explains the bending of NC-2. In Fig. 7(c), $(200)_{CdO}$ plane is parallel to $(10\bar{1}1)_{CdS}$ plane while $[010]_{CdO}$ zone axis is parallel to $[\bar{1}2\bar{1}0]_{CdS}$ zone axis. For NC-3, five $(002)_{CdO}$ layers match to four $(0002)_{CdS}$ layers on the interface with an angle of 29.5 °. In Fig. 7(d), $(002)_{CdO}$ plane is parallel to $(10\bar{1}1)_{CdS}$ plane while $(111)_{CdO}$ plane is parallel to $(10\bar{1}\bar{1})_{CdS}$ plane, and $[1\bar{1}0]_{CdO}$ zone axis is parallel to $[\bar{1}2\bar{1}0]_{CdS}$ zone axis. For NC-4, five $(11\bar{1})_{CdO}$ layers match to four $(0002)_{CdS}$ layers on the interface with an angle of 4.0 °. Interestingly, the angle between $(002)_{CdO}$ plane and $(111)_{CdO}$ plane (54.7 °) is close to that between $(10\bar{1}1)_{CdS}$ plane and $(10\bar{1}\bar{1})_{CdS}$ plane (56.4 °), which may contribute to the formation of this interface structure. In Fig. 7(e), $(111)_{CdO}$ plane is parallel to $(10\bar{1}0)_{CdS}$ plane while $[1\bar{1}0]_{CdO}$ zone axis is parallel to $[\bar{1}2\bar{1}0]_{CdS}$ zone axis. For NC-5, seven $(002)_{CdO}$ layers match to six $(0002)_{CdS}$ layers on the interface with an angle of 35.0 °. In Fig. 7(f), $(002)_{CdO}$ plane is parallel to the $(10\bar{1}0)_{CdS}$ plane while $(220)_{CdO}$ plane is parallel to $(0002)_{CdS}$ plane, and $[1\bar{1}0]_{CdO}$ zone axis is parallel to $[\bar{1}2\bar{1}0]_{CdS}$ zone axis. For NC-6, two $(220)_{CdO}$ layers match to one $(0002)_{CdS}$ layers on the interface. According to the statistical analysis of the orientation distribution of thirty CdO nanocrystals (Fig. S13 in the ESM), the {002} plane of CdO tends to be parallel or perpendicular to the $\{10\bar{1}0\}$ plane of CdS. Therefore, the heterojunction interfaces corresponding to NC-1, NC-2, and NC-6 are more advantageous in six nonequivalent heterojunction interfaces, and the heterojunction interface corresponding to NC-2 ($(002)_{CdO}$ plane is perpendicular to $(10\bar{1}0)_{CdS}$ plane while $(200)_{CdO}$ plane is parallel to $(10\bar{1}0)_{CdS}$ plane) may be the most advantageous one. Considering the above, the CdO nanocrystals nucleate and grow at surface defects. They effectively fill the lattice defect structure of CdS matrix, and appropriate interface lattice matching is formed between CdO nanocrystals and CdS surface to reduce interface energy.

4 Conclusions

In summary, the nucleation and growth mechanism of CdO

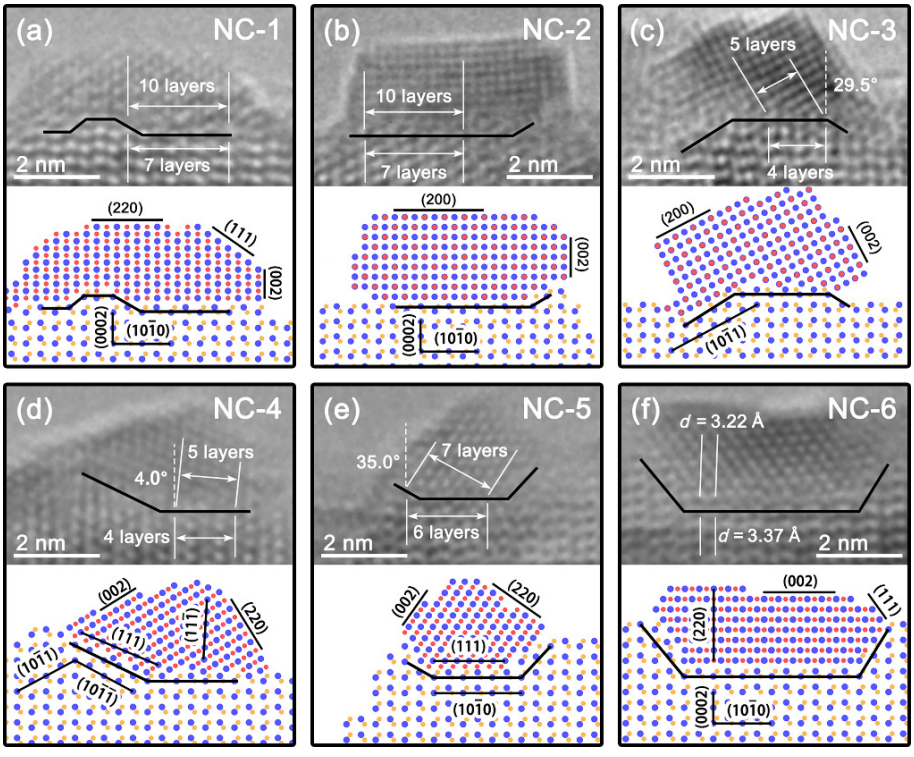

Figure 7 HRTEM images and atomic models of six RS CdO nanocrystals with different crystal orientations on WZ CdS matrix: (a) NC-1, (b) NC-2, (c) NC-3, (d) NC-4, (e) NC-5, and (f) NC-6.

nanocrystals based on electron beam induced surface oxidation of CdS is studied in this work. *In situ* TEM observation reveals the structural evolution of CdS nanowires induced by electron beam irradiation, which accompanied by the decomposition of CdS nanowires and the formation of CdO nanocrystals. The results of EDS indicate the element exchange between the CdS nanowires and the column vacuum of TEM during the electron beam irradiation. The CdO nuclei nucleate through a non-classical two-step nucleation path on CdS surface. Amorphous clusters are formed firstly as the intermediate phase on CdS surface, then CdO nuclei appear in the amorphous phase. Reversible disorder–order transitions of CdO nucleus are observed in the early crystal nucleation stage. Then, the CdO nucleus grows rapidly by absorbing excess amorphous phase. The layer-by-layer growth of $(002)_{CdO}$ plane is observed in subsequent crystal growth process. Additionally, six nonequivalent heterojunction interface orientation relationships between CdO nanocrystals and CdS matrix are deeply analyzed by building atomic models. Surface defects may be an important factor affecting the oriented growth of CdO nanocrystals. And appropriate interface lattice matching is formed between CdO nanocrystals and CdS matrix. This work has potential application prospects for atomic manufacturing and interface control of semiconductor heterojunction.

Electronic Supplementary Material: Supplementary material (XRD spectrum, SEM images, EDS spectra, extra TEM images, and movies) is available in the online version of this article at https://doi.org/10.26599/NR.2025.94907001.

Data availability

All data needed to support the conclusions in the paper are presented in the manuscript and the Electronic Supplementary Material. Additional data related to this paper may be requested from the corresponding author upon request.

Acknowledgements

This work was financially supported by the National Key R&D Program of China (No. 2019YFA0210003) and the National Natural Science Foundation of China (No. 12275201). Thanks to Dr. Xiaoxiao Zhang, Mrs. Ke Zhang, and Prof. Yi Xiong from the Analytical and Testing Center of Wuhan Textile University for their technical support.

Declaration of competing interest

All the contributing authors report no conflict of interests in this work.

Author contribution statement

Y. M. W.: Conceptualization, formal analysis, investigation, methodology, writing – original draft. Y. X.: Resources, writing – review & editing. W. Z.: Writing – review & editing; P. F. F.: Project administration, supervision, funding acquisition, resources, writing – review & editing.

Use of AI statement

None.

References

[1] Han, Q.; Han, Z. W.; Wang, Y. M.; Zhang, S. Y.; Fang, J. P.; Li, H. J.; Fang, P. F. Enhanced photocatalytic hydrogen evolution by piezoelectric effects based on $MoSe_2$/Se-decorated CdS nanowire edge-on heterostructure. *J. Colloid Interface Sci.* **2023**, *630*, 460–472.

[2] Zhang, S. Y.; Du, S. W.; Wang, Y. M.; Han, Z. W.; Li, X.; Li, G. J.; Hu, Q.; Xu, H.; He, C. Q.; Fang, P. F. Synergy of yolk-shelled structure and tunable oxygen defect over CdS/$CdCO_3$-CoS_2: Wide band-gap semiconductors assist in efficient visible-light-driven H_2 production and CO_2 reduction. *Chem. Eng. J.* **2023**, *454*, 140113.

[3] Dang, T. H.; Khalili, A.; Abadie, C.; Gréboval, C.; Cavallo, M.; Zhang, H. C.; Bossavit, E.; Utterback, J. K.; Dandeu, E.; Prado, Y. et al. Nanocrystal-based active photonics device through spatial design of light-matter coupling. *ACS Photonics* **2022**, *9*, 2528–2535.

[4] Li, J. R.; Wang, Z. M.; Zhang, H.; Gao, J.; Zheng, A. P. Progress in the development of stabilization strategies for nanocrystal preparations. *Drug Deliv.* **2021**, *28*, 19–36.

[5] Zhang, P.; Yu, X.; Xia, P.; Cui, Z. Z.; Yi, J. H.; Li, C. J.; Song, P.; Zhao, F.; Wang, T.; Qiu, J. B. et al. Real-time evolution of up-conversion nanocrystals from tailored metastable intermediates. *Nano Res.* **2023**, *16*, 1552–1557.

[6] Zhan, H. Q.; Deng, C.; Shi, X. L.; Wu, C. Q.; Li, X. H.; Xie, Z. P.; Wang, C. A.; Chen, Z. G. Correlation between the photocatalysis and growth mechanism of SnO_2 nanocrystals. *J. Phys. D: Appl. Phys.* **2020**, *53*, 154005.

[7] Brown, A. A. M.; Vashishtha, P.; Hooper, T. J. N.; Ng, Y. F.; Nutan, G. V.; Fang, Y. A.; Giovanni, D.; Tey, J. N.; Jiang, L. D.; Damodaran, B. et al. Precise control of $CsPbBr_3$ perovskite nanocrystal growth at room temperature: Size tunability and synthetic insights. *Chem. Mater.* **2021**, *33*, 2387–2397.

[8] Xiong, Y.; Li, H. J.; Zeng, W.; Wang, Y. M.; Zhao, X. N.; Fang, P. F.; Hu, W. G.; Zheng, L. R. Lattice origin of few-layer edge-on MoS_2@TiO_2 octahedral clusters for piezoelectric enhancement. *Appl. Surf. Sci.* **2022**, *588*, 152942.

[9] Ondry, J. C.; Philbin, J. P.; Lostica, M.; Rabani, E.; Alivisatos, A. P. Resilient pathways to atomic attachment of quantum dot dimers and artificial solids from faceted CdSe quantum dot building blocks. *ACS Nano* **2019**, *13*, 12322–12344.

[10] Nie, X.; Xiong, Y.; Zeng, W. The interfacial lattice origin of anatase titanium dioxide by hydrothermal architecture. *J. Cryst. Growth* **2020**, *552*, 125927.

[11] Karthika, S.; Radhakrishnan, T. K.; Kalaichelvi, P. A review of classical and nonclassical nucleation theories. *Cryst. Growth Des.* **2016**, *16*, 6663–6681.

[12] Jun, Y. S.; Zhu, Y. G.; Wang, Y.; Ghim, D.; Wu, X. H.; Kim, D.; Jung, H. Classical and nonclassical nucleation and growth mechanisms for nanoparticle formation. *Annu. Rev. Phys. Chem.* **2022**, *73*, 453–477.

[13] Fu, H. Y.; Gao, X.; Zhang, X.; Ling, L. Recent advances in nonclassical crystallization: Fundamentals, applications, and challenges. *Cryst. Growth Des.* **2022**, *22*, 1476–1499.

[14] Jin, B.; Liu, Z. M.; Tang, R. K. Recent experimental explorations of non-classical nucleation. *Crystengcomm* **2020**, *22*, 4057–4073.

[15] Chakrabortty, S.; Guchhait, A.; Ong, X.; Mishra, N.; Wu, W. Y.; Jhon, M. H.; Chan, Y. Facet to facet linking of shape anisotropic inorganic nanocrystals with site specific and stoichiometric control. *Nano Lett.* **2016**, *16*, 6431–6436.

[16] Coropceanu, I.; Janke, E. M.; Portner, J.; Haubold, D.; Nguyen, T. D.; Das, A.; Tanner, C. P. N.; Utterback, J. K.; Teitelbaum, S. W.; Hudson, M. H. et al. Self-assembly of nanocrystals into strongly electronically coupled all-inorganic supercrystals. *Science* **2022**, *375*, 1422–1426.

[17] Shi, R. P.; Heo, T. W.; Wood, B. C.; Wang, Y. Z. Critical nuclei at hetero-phase interfaces. *Acta Mater.* **2020**, *200*, 510–525.

[18] Houben, L.; Weissman, H.; Wolf, S. G.; Rybtchinski, B. A mechanism of ferritin crystallization revealed by cryo-STEM tomography. *Nature* **2020**, *579*, 540–543.
[19] Tao, F.; Han, Q.; Deng, M. R.; Miao, S. T.; Yang, P. pH-responsive protein conformation transistor. *Angew. Chem., Int. Ed.* **2024**, *63*, e202310879.
[20] Dighe, A. V.; Coliaie, P.; Podupu, P. K. R.; Singh, M. R. Selective desolvation in two-step nucleation mechanism steers crystal structure formation. *Nanoscale* **2022**, *14*, 1723–1732.
[21] Yang, S.; Guo, Z. Z.; Bian, B. R.; Du, J.; Hu, Y. Dynamic observation of anisotropic chainlike structures during nonclassical two-step nucleation in solid-state iron oxide crystallization. *J. Phys. Chem. Lett.* **2022**, *13*, 8352–8358.
[22] Cao, K. C.; Biskupek, J.; Stoppiello, C. T.; McSweeney, R. L.; Chamberlain, T. W.; Liu, Z.; Suenaga, K.; Skowron, S. T.; Besley, E.; Khlobystov, A. N. et al. Atomic mechanism of metal crystal nucleus formation in a single-walled carbon nanotube. *Nat. Chem.* **2020**, *12*, 921–928.
[23] Kim, H. J.; Kim, J. H.; Jeong, J. S.; Moon, C. Y.; Nahm, S.; Nam, K. M.; Park, J.; Kim, Y. H. Heterointerface effect on two-step nucleation mechanism of bi particles. *Nano Lett.* **2022**, *22*, 3252–3259.
[24] Zhang, H. T.; Wang, W.; Xu, T.; Xu, F.; Sun, L. T. Phase transformation at controlled locations in nanowires by *in situ* electron irradiation. *Nano Res.* **2020**, *13*, 1912–1919.
[25] Ting, Y. H.; Wu, M. C.; Aoyama, Y.; Lu, K. C.; Wu, W. W. *In situ* manipulation of E-beam irradiation-induced nanopore formation on molybdenum oxide nanowires. *Appl. Surf. Sci.* **2021**, *544*, 148874.
[26] Li, J. J.; Deepak, F. L. *In situ* generation of sub-10 nm silver nanowires under electron beam irradiation in a TEM. *Chem. Commun.* **2020**, *56*, 4765–4768.
[27] Yasuda, H. Fast *in situ* ultrahigh-voltage electron microscopy observation of crystal nucleation and growth in amorphous antimony nanoparticles. *Cryst. Growth Des.* **2018**, *18*, 3302–3306.
[28] Sheng, H. P.; Zheng, H.; Jia, S. F.; Chan, M. K. Y.; Rajh, T.; Wang, J. B.; Wen, J. G. Atomistic manipulation of reversible oxidation and reduction in Ag with an electron beam. *Nanoscale* **2019**, *11*, 10756–10762.
[29] Su, Q. M.; Du, G. H.; Xu, B. S. *In situ* growth of In_2O_3 nanocrystals by electron irradiation in transmission electron microscope. *Mater. Lett.* **2014**, *120*, 208–211.
[30] Gonzalez-Martinez, I. G.; Bachmatiuk, A.; Bezugly, V.; Kunstmann, J.; Gemming, T.; Liu, Z.; Cuniberti, G.; Rümmeli, M. H. Electron-beam induced synthesis of nanostructures: A review. *Nanoscale* **2016**, *8*, 11340–11362.
[31] Yang, K. H.; Yang, Z. Z.; Zhang, C.; Gu, Y. L.; Wei, J. J.; Li, Z. H.; Ma, C.; Yang, X.; Song, K. X.; Li, Y. M. et al. Recent advances in CdS-based photocatalysts for CO_2 photocatalytic conversion. *Chem. Eng. J.* **2021**, *418*, 129344.
[32] Marder, A. A.; Cassidy, J.; Harankahage, D.; Beavon, J.; Gutiérrez-Arzaluz, L.; Mohammed, O. F.; Mishra, A.; Adams, A. C.; Slinker, J. D.; Hu, Z. J. et al. CdS/CdSe/CdS spherical quantum wells with near-unity biexciton quantum yield for light-emitting-device applications. *ACS Mater. Lett.* **2023**, *5*, 1411–1419.
[33] Gao, Y. B.; Kong, D. H.; Han, J. Y.; Zhou, W. R.; Gao, Y.; Wang, T. S.; Lu, G. Y. Cadmium sulfide *in-situ* derived heterostructure hybrids with tunable component ratio for highly sensitive and selective detection of ppb-level H_2S. *J. Colloid Interface Sci.* **2022**, *627*, 332–342.
[34] Li, C. H.; Hsu, C. W.; Lu, S. Y. TiO_2 nanocrystals decorated Z-schemed core-shell CdS-CdO nanorod arrays as high efficiency anodes for photoelectrochemical hydrogen generation. *J. Colloid Interface Sci.* **2018**, *521*, 216–225.
[35] Saha, M.; Ghosh, S.; De, S. K. Nanoscale kirkendall effect driven Au decorated CdS/CdO colloidal nanocomposites for efficient hydrogen evolution, photocatalytic dye degradation and Cr (VI) reduction. *Catal. Today* **2020**, *340*, 253–267.
[36] Huang, X.; Jones, T.; Fan, H.; Willinger, M. G. Atomic-scale observation of irradiation-induced surface oxidation by *in situ* transmission electron microscopy. *Adv. Mater. Interfaces* **2016**, *3*, 1600751.
[37] Li, C. H.; Wang, H. M.; Naghadeh, S. B.; Zhang, J. Z.; Fang, P. F. Visible light driven hydrogen evolution by photocatalytic reforming of lignin and lactic acid using one-dimensional NiS/CdS nanostructures. *Appl. Catal. B: Environ.* **2018**, *227*, 229–239.
[38] Peterson, K. A.; Shepler, B. C.; Singleton, J. M. The group 12 metal chalcogenides: An accurate multireference configuration interaction and coupled cluster study. *Mol. Phys.* **2007**, *105*, 1139–1155.
[39] Yang, J.; Koo, J.; Kim, S.; Jeon, S.; Choi, B. K.; Kwon, S.; Kim, J.; Kim, B. H.; Lee, W. C.; Lee, W. B. et al. Amorphous-phase-mediated crystallization of Ni nanocrystals revealed by high-resolution liquid-phase electron microscopy. *J. Am. Chem. Soc.* **2019**, *141*, 763–768.
[40] Li, J. J.; Li, Q.; Wang, Z. C.; Deepak, F. L. Real-time dynamical observation of lattice induced nucleation and growth in interfacial solid-solid phase transitions. *Cryst. Growth Des.* **2016**, *16*, 7256–7262.
[41] Giacopetti, L.; Nevin, A.; Comelli, D.; Valentini, G.; Nardelli, M. B.; Satta, A. First principles study of the optical emission of cadmium yellow: Role of cadmium vacancies. *AIP Adv.* **2018**, *8*, 065202.
[42] Roehl, J. L.; Liu, Z. T. Y.; Khare, S. V. Diffusion in CdS of Cd and S vacancies and Cu, Cd, Cl, S and Te interstitials studied with first-principles computations. *Mater. Res. Express* **2014**, *1*, 025904.
[43] Jeon, S.; Heo, T.; Hwang, S. Y.; Ciston, J.; Bustillo, K. C.; Reed, B. W.; Ham, J.; Kang, S.; Kim, S.; Lim, J. et al. Reversible disorder-order transitions in atomic crystal nucleation. *Science* **2021**, *371*, 498–503.